Engineering Structures 212 (2020) 110469

Contents lists available at ScienceDirect

Engineering Structures

journal homepage: www.elsevier.com/locate/engstruct

Elastic buckling behaviour of Σ-shaped rack columns under uniaxial compression

Peng Zhang, M. Shahria Alam*

School of Engineering, Univ. of British Columbia, 3333 University Way, Kelowna, British Columbia V1V 1V7, Canada

ARTICLE INFO

Keywords:
Rack column
Perforation
Elastic buckling
Compression
Buckling curve

ABSTRACT

Elastic buckling properties of thin-walled storage rack columns under compression, e.g., critical buckling loads, are often the input parameters for analytical design solutions (e.g., the direct strength method in AISI_S100 2016). This paper deals with the accurate estimation of the elastic buckling properties of Σ-shaped rack sections with patterned holes. The investigation of the elastic buckling behaviour of three different Σ-shaped rack sections (with and without patterned holes) under compression is presented. More than 4000 finite element simulations were performed on these rack sections using the finite element program, ANSYS 18.1. The influences of the holes, perforation pattern, number of buckling half-wavelengths, and boundary conditions on the section' buckling behaviour were studied. An alternative method is proposed to generate signature curves for solid rack sections, and its effectiveness has been tested to generate signature curves for perforated rack sections. Multi-half-wavelengths method is proposed to determine the critical buckling loads and critical buckling half-wavelengths of perforated rack sections, which has been proved to be unbiased and accurate. The results show that by considering the holes, the critical buckling loads of the rack sections decreased while the critical buckling half-wavelengths increased. The alternative method failed to generate the signature curves of perforated rack sections accurately since the shape functions used for describing the shapes of buckling modes of perforated rack columns are significantly different from those used for solid rack sections.

1. Introduction

Rack columns are generally made of thin-walled steel sheets, and the steel sheets are cold-formed into the desired sections of the columns. The columns are used to form the upright frames of a storage system and serve as compression members. To simplify the assembly of the upright frames and make the intervals of shelf panels adjustable, holes are often made at webs or flanges of rack columns along the length uniformly.

Most rack columns have open and singly symmetric cross-sections. It imposes difficulties on structural designers for designing such columns, especially for perforated rack columns. This is because multiple buckling modes need to be considered for rack columns in the design. The common buckling modes of Local (L), Distortional (D), Torsional + Flexural (TF), and Flexural (F) buckling are shown in Fig. 1, and their definitions are given in the AISI_S100 [1]. The flexural buckling mode around the strong principal axis of the rack section is not available since the flexural buckling modes around the strong principal axis are always accompanied by torsional buckling mode due to the singly symmetric cross-section. TF and F buckling usually jointly termed as Global (G) buckling. In a compression test, these buckling modes may happen on a column simultaneously or at different loading points, and hence the column presents interactive buckling modes, e.g., L + D, L + G, D + G, and L + D + G [2–5]. The second reason is that the CUFSM v4.05 [6] and GBTUL 2.0 [7] are user-friendly computer programs for determining the elastic buckling properties of solid rack columns; however, they cannot handle perforated columns directly.

The study of the buckling behaviour of rack columns under compression can be traced back to 1980s. In 1984, Hancock [8] experimentally explored the distortional buckling behaviour of rack columns under compression. It was observed that distortional buckling interacted with material yielding and resulted in the ultimate loads of columns lower than their elastic distortional buckling loads. In 1986, Hancock and Roos [9] investigated the TF buckling behaviour of two solid rack columns. The columns were assembled in a single span of upright frame and then were compressed axially till failure. It was observed that the column compression capacity was significantly decreased after losing the tightness of column-brace joints. In 1997, Davies et al. [10] experimentally studied the buckling behaviour of two types of perforated rack columns under compression. For considering

* Corresponding author.
E-mail addresses: p.zhang@alumni.ubc.ca (P. Zhang), shahria.alam@ubc.ca (M.S. Alam).

https://doi.org/10.1016/j.engstruct.2020.110469
Received 31 January 2019; Received in revised form 8 October 2019; Accepted 3 March 2020

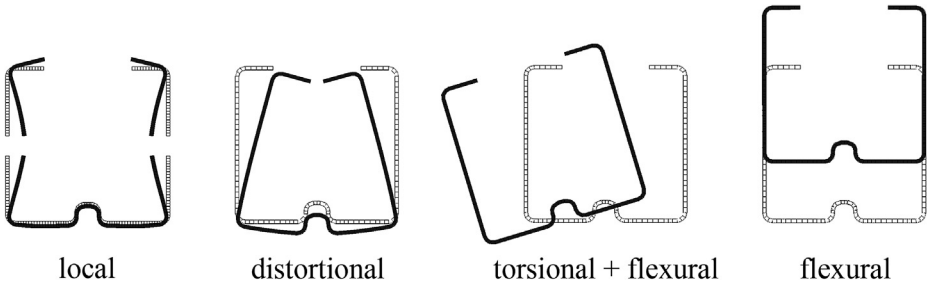

Fig. 1. Cross-sectional deformation of different buckling modes.

holes, the effective thickness method was proposed and employed with the Generalized Beam Theory (GBT) to predict the compression capacity of columns. In 2004, Yang and Hancock [2] physically tested solid and high-strength rack columns under compression. The results showed that for columns experiencing local and distortional interactive buckling, columns with flanges deformed inward had lower compression capacities than those columns with flanges deformed outward. Buckling shapes had almost no influences on the compression capacity of those columns subjected to local buckling. In 2011, the buckling behaviour of perforated rack columns under compression was experimentally studied by Casafont et al. [4]. It was found that distortional buckling modes of the columns always accompanied by global buckling mode. Interactions of buckling modes affected the compression capacity of columns, and the effects varied with the column length. In 2011, Casafont et al. [11] experimentally evaluated the accuracy of the Direct Strength Method (DSM) (in AISI_S100 2007) for predicting the compression capacity of perforated rack columns. Results showed that by considering the actual boundary conditions of columns in determining critical distortional buckling loads, the accuracy of the DSM improved. Nevertheless, the DSM still had large errors in many columns. In 2014, Dinis et al. [5] experimentally investigated the local and distortional interactive buckling behaviour of solid rack columns. It was observed that interactive buckling modes of L + D happened on those columns with critical local buckling loads lower than critical distortional buckling loads by 30% to 46%. In 2016, Yao and Rasmussen [12] proposed an analytical design solution (Proposed Method 2), which was claimed to be capable of designing perforated thin-walled columns with multiple shapes of cross-sections subject to compression.

From the literature review, two conclusions can be made. The first conclusion is that analytical design solutions for predicting the compression capacity of Σ-shaped and perforated rack columns are not mature yet. The DSM in the AISI_S100 [1] may lack the accuracy when applied to Σ-shaped rack columns because it was developed for columns with lipped-channel cross-sections [13]. The second conclusion is that it is necessary to propose an accurate and unbiased method for determining the critical buckling loads and critical buckling half-wavelengths of perforated rack sections since these parameters are often used as input parameters for analytical design solutions, e.g., the DSM [1]. This paper presents a theoretical study, which investigates the elastic buckling behaviour of Σ-shaped rack sections with and without patterned holes. Research [14,15] shows that the compression capacity of thin-walled columns is affected by initial geometric imperfections, cold-forming effects (residual stresses and strength enhancements of the material at corners) , and material nonlinearities (e.g., yielding and strain hardening). However, this study only investigates the elastic buckling behaviour. In this paper, four problems are identified as shown in Table 1. While dealing with problem (a), the differences of the elastic buckling behaviour (local, distortional, and global buckling) between perforated and nonperforated Σ-shaped rack sections are numerically investigated thoroughly in this paper. Understanding these differences is critical for developing proper design solutions for perforated rack columns under compression. For problem (b), it is demonstrated in this paper that trigonometric shape functions are not applicable to describe the shape of buckling modes of perforated rack columns. It is critical to acknowledge this since in recent years, scientists [11,16] proposed simplified solutions for determining critical elastic buckling loads for perforated rack columns using finite strip method. The finite strip method [6] adopts trigonometric functions as shape functions. To address the problem (c), the multi-half-wavelengths method is proposed in this paper, which can accurately determine the critical buckling half-wavelength and critical buckling load of local and distortional buckling of perforated rack columns. This method can be a robust tool for developing and/or validating simplified analytical/numerical solutions for determining the critical buckling load and the critical buckling half-wavelength of perforated rack columns. For the problem (d), it is demonstrated in the paper that the pinned-pinned boundary condition fails to consider the multi-half-wavelengths effect of rack columns under compression. The pinned-pinned boundary condition is widely used by the scientists [4,17–20] for experimentally test perforated and nonperforated rack columns under compression, and analytical design solutions were developed based on those results.

2. Specimens

2.1. Column profiles

Three different rack columns in North America were selected for this study. The profile of columns and their nominal net cross-sections are shown in Fig. 2. Along the length, patterned holes are uniformly made at the flanges, webs, and intermediate stiffener of these columns. The net cross-section of a perforated column is the cross-section that has the minimum area along the length. The dimensions of column nominal cross-sections are shown in Table 2, and these dimensions were measured along the outer face of cross-sections while the corner radii were measured along the middle face of cross-sections. The columns have the same thickness of 1.80mm, and all the corners of cross-sections are right angles.

2.2. Material properties

Material properties of the columns were determined experimentally and are presented in [21]; Here, the results of Young's modulus (E) are only shown in Table 3.

3. Generation and validation of numerical models

In this section, numerical models generated using computer programs of CUFSM v4.05 [6] and ANSYS 18.1 [22] are validated using experimental results. The generation of Finite Element (FE) models in ANSYS 18.1 [22] is described in detail. It is worth mentioning that more than 4000 finite element models of rack columns (including the numerical models used for experimental validation) were generated in this study. Eigenbuckling analyses were performed on these numerical models for generating buckling curves and signature curves of the rack sections. It was tedious to generate signature curves of solid rack sections due to the employment of constraint equations on the numerical

Table 1
Problems addressed in the paper and the corresponding sections.

No.	Problems	Sections
(a)	What the differences are between the buckling behaviour of solid and perforated rack columns.	4.2 and 5.2
(b)	Whether the shape functions used for describing the shapes of buckling modes of solid rack columns fit the perforated rack columns.	5.2
(c)	How the critical buckling loads and critical buckling half-wavelengths of perforated rack sections can be determined accurately.	4.4, 5.1, and 5.4
(d)	Whether the pinned–pinned boundary condition is suitable to be used in experiments for determining the compression capacity of rack columns.	5.3

models. To obtain one of the signature curves, 50 to 70 h were required for generating the corresponding numerical models and performing eigenbuckling analyses. Computers with Intel(R) Core(TM) i7 processor, 4 cores, and 16.0 GB RAMs were used to run the simulations. The generation of buckling curves and signature curves of perforated rack sections was much more tedious than those of the nonperforated rack sections since different perforation patterns had to be considered at each length. It took more than a month to generate one of the buckling curves/signature curves of the perforated rack sections.

3.1. Buckling curve and signature curve

Eigenbuckling analyses of rack columns are often performed by engineers or scientists. The results of eigenbuckling analyses have a certain degree of accuracy on the prediction of buckling modes of rack columns. While predicting the compression capacity of rack columns, more factors need to be considered such as initial geometric imperfections and material nonlinearities. From eigenbuckling analyses results, two important characteristics: Buckling Curve (BC) and Signature Curve (SC) can be obtained [2,3,8,11,13,23]. The BC shows a section's lowest elastic buckling load (corresponding to the 1st buckling mode) against length under a given boundary condition. The Signature Curve (SC) is proposed to quickly determine critical buckling loads and critical buckling half-wavelengths of thin-walled sections. To generate an SC, constraints or shape functions are applied in column models so that shapes of buckling modes vary in a sinusoidal way along the length [24].

3.2. Boundary condition

In structural design, the boundary conditions of rack columns are generally idealized as Simply-Simply ($S-S$) or Clamped-Clamped ($C-C$) boundary conditions. For the $S-S$ boundary condition, the transverse displacements of column ends are restrained while the column ends are free to warp. For the $C-C$ boundary condition, column ends are fixed except one of the ends (the loading end) can move longitudinally in the form of rigid-body movements.

3.3. Finite element models

In ANSYS 18.1 [22], the accuracy of the Shell63 element and Shell181 element on eigenbuckling analysis was compared. It was found that the Shell63 element provided closer results when compared to those of the CUFSM v4.05 [6] than the Shell181 element. Hence, Shell63 element was selected in this study. The Shell63 element was also adopted by Casafont et al. [11] for performing eigenbuckling analysis of rack columns. An FE model with Section COOOI (shown in Fig. 3(a)) under the $S-S$ boundary condition is shown in Fig. 3(b). At the two ends of the model, the U_x and U_y of all the nodes are restrained, and a uniform compressive load is applied to them. Moreover, the U_z of one node at the centre of the web of the central cross-section is restrained. Fig. 3(c) presents an FE model under the $C-C$ boundary condition. In this figure, at the loading end (left end), all the degrees of freedom of the nodes are restrained except that the U_z is coupled to allow only rigid-body movements. All the degrees of freedom of the nodes at the right end are restrained. For all the models, the size of 2 mm was selected for meshing the cross-sections. Along the length of the models, the meshing sizes of 1 mm, 2 mm, and 4 mm were used for the cases presenting L, D, and TF buckling, respectively.

3.4. Validation of numerical models

Two rack specimens with the section COOOI and the length of 900 mm were experimentally investigated by Hancock [8]. Cross-sectional dimensions of the specimens [8] are presented in Table 4. In the tests, the specimens failed elastically under uniaxial compression and presented distortional buckling modes with two half-wavelengths [8]. The ultimate loads and ultimate strength of the specimens [8] are shown in Table 5.

Eigenbuckling analyses were performed on the two rack specimens using the two computer programs. The $S-S$ boundary condition was applied to the numerical models. In the tests, the specimens were compressed between rigid platens. The friction generated between the rigid platens and the ends of the specimens could effectively restrain the transverse displacements of the ends of the specimens while the warping was not possible to be restrained. The elastic buckling stresses of the specimens yielded from the two computer programs are compared with the experimental results as presented in Table 5. For the specimen D1, the elastic buckling stresses yielded from the two computer programs are very close to the experimental ultimate strength where only 1% differences were found between them. For the specimen D2, the elastic buckling stresses obtained from the two computer programs are 7% greater than the experimental ultimate strength. It is noted that the ultimate strength of the specimen D2 is 7.9% lower than that of the specimen D1, which indicates that the specimen D2 probably had larger initial geometric imperfections than the specimen D1. It was

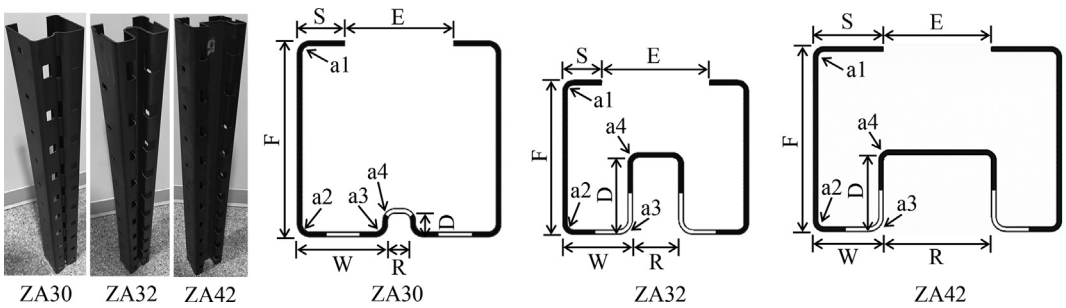

Fig. 2. Column profiles.

Table 2
Dimensions of column nominal cross-sections.

Column	Dimension (mm)						Radius (mm)				Area (mm^2)	
	S	F	W	R	D	E	a1	a2	a3	a4	A_{net}	A_{gross}
ZA30	19.05	79.38	36.51	9.53	9.53	44.45	4.08				432.75	499.97
ZA32	19.05	63.50	28.58	19.05	31.8	38.10	3.44	3.44	4.96	3.44	408.53	512.06
ZA42	28.58	76.20	28.58	44.45	31.8	44.45	3.44	3.44	4.97	3.44	534.26	637.78

Table 3
Column material property.

Column	ZA30	ZA32	ZA42
E ($\times 10^5 MPa$)	2.06	2.08	2.06

observed that the buckling modes yielded from the two computer programs agreed well with the failure modes of the specimens. The buckling mode of the specimen D1 yielded from the ANSYS 18.1 [22] is presented in Fig. 4(a).

Buckling curves of the section COOOI (with the geometries of the specimen D1) under the $S-S$ and $C-C$ boundary conditions were generated using the two computer programs. The length range of the buckling curves was defined from $30mm$ to $4000mm$ so that the performance of the numerical models for dealing with different kinds of buckling modes of L, D, and TF can be evaluated. The buckling curves under the $S-S$ and $C-C$ boundary conditions generated using the ANSYS 18.1 [22] are plotted against the corresponding buckling curves generated using the CUFSM v4.05 [6] in Fig. 4(a) and (b), respectively. Good agreements between the curves can be observed in these figures. The differences between the results (elastic buckling stresses) yielded from the two computer programs are within ± 2%, and the buckling modes mutually agreed.

4. Buckling behaviour of solid rack columns

In this section, the BCs and SCs of three solid Σ-shaped sections were generated using ANSYS 18.1 [22] and CUFSM v4.05 [6].

4.1. Generation of the BC and SC

The procedures for generating BCs of the rack sections were the same as those introduced in Section 3. For generating the SCs of the rack sections, constraint equations were imposed on FEM models. This method was motivated by Casafont et al. [11] and is described in detail here. The invention of constraint equations was referred to the shape functions adopted in the FSM [6]. In the FSM, a model is discretized only in the cross-section, and hence the model looks like consisted of many longitudinal strips. Each strip is a single element in the model. The trigonometric function of $u = sin(\pi Z/L)$ (adopted for models under the $S-S$ boundary condition) and $u = sin(\pi Z/L)^2$ (adopted for models under the $C-C$ boundary condition) are adopted in the FSM to describe the membrane deformation and out-of-plane displacement of the strip in the longitudinal direction [6,24].

In the ANSYS 18.1 [22], the depth/width ratios of elements were controlled to be ≤ 3. Sizes among $1.5mm$ to $3mm$ were used to mesh the cross-sections of models. In the longitudinal direction, meshing sizes among $1.5mm$ to $6mm$ were used. The longer the models, the larger the meshing sizes. For generating the SCs (under the $S-S$ boundary condition) of the rack sections, half-length models and the SYMM boundary condition were used for efficiency. Multiple nodal lines were selected in the FEM models, and a constraint equation (Eq. (1)) was applied to the nodal lines. The selected nodal lines are marked with red arrows and are shown in Fig. 5. The nodal lines were selected such that the deformation of the whole cross-sections can be effectively constrained and the generation of membrane stresses in the plane of the cross-sections due to the constraint can be avoided. In each nodal line, the node at the cross-section where the SYMM boundary condition is applied to is the master node, and the rest of the nodes are the slave nodes. Since the master node has the maximum out-of-plane displacement in each nodal line, it is convenient to assume that the maximum displacement to be unity ($u_m = 1$). Eq. (1), consequently, can be converted into Eq. (2). For generating the SCs (under the $C-C$ boundary condition) of the rack sections, full-length models were employed, and Eq. (3) was employed as the constraint equation. In each nodal line, the master node is located at the length centre. Likewise, Eq. (3) can be converted to Eq. (4) when the u_m is assumed to be unity. An FEM model of the ZA32 section with the constraint equation applied is presented in Fig. 5(d) as an illustration. In this model, the nodes at the two ends are excluded from the slave nodes since boundary conditions are applied here.

$$u_s sin(\pi Z_m/L + \pi/2) - u_m sin(\pi Z_s/L + \pi/2) = 0 \quad (1)$$

$$u_s = sin(\pi Z_s/L + \pi/2) \quad (2)$$

$$u_s sin^2(\pi Z_m/L) - u_m sin^2(L) = 0 \quad (3)$$

$$u_s = sin^2(\pi Z_s/L) \quad (4)$$

u_s – out-of-plane displacement of the slave node.
u_m – out-of-plane displacement of the master node.
Z_s–Z coordinate of the slave node in the models. $Z_s > 0$.
Z_m–Z coordinate of the master node in the models. $Z_m \geq 0$.

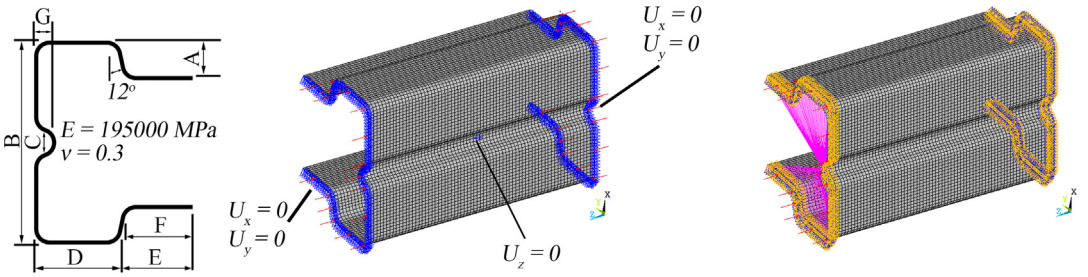

(a) Section COOOI (b) FE model under the S-S boundary condition (c) FE model under the C-C boundary condition

Fig. 3. Cross-sectional profile and finite element models.

Table 4
Measured specimen dimensions of section COOOI.

Specimen	t (*mm*)	A (*mm*)	B (*mm*)	C (mm)	D (*mm*)	E (*mm*)	F (*mm*)	G (*mm*)	Area(mm^2)
D1	1.625	15.575	89.600	9.465	38.500	31.164	29.811	7.875	401.030
D2	1.630	15.170	89.500	9.492	38.400	31.672	30.406	7.970	402.557

Table 5
Failure stresses of specimens with section COOOI.

Specimen	Experimental results		Elastic buckling stress(*MPa*)		Stress ratio	
	Ultimate load(*kN*)	Ultimate stress(*MPa*)	FSM	FEM	FSM/Exp	FEM/Exp
D1	100.8	252.0	249.2	250.5	0.99	0.99
D2	92.9	232.0	247.4	248.7	1.07	1.07

L – full length of the model.

For the FE models under the $S-S$ boundary condition, the SYMM boundary condition was applied to the cross-section of $Z=0$. The plane $Z=0$ can be at any of the ends of the models under the $C-C$ boundary condition.

4.2. Bcs and SCs of solid rack sections

The SCs and BCs of the three solid rack sections are shown in Figs. 6–8. For the BCs in the figures: (1) column buckling modes are indicated; (2) boundaries between adjacent two different buckling modes are presented; and (3) few column buckling modes are selected and shown in the right side of the figures. The critical half-wavelengths and critical buckling loads are symbolized as (l_{crl}^{S-S}, P_{crl}^{S-S}), (l_{crd}^{S-S}, P_{crd}^{S-S}), (l_{crl}^{C-C}, P_{crl}^{C-C}), and (l_{crd}^{C-C}, P_{crd}^{C-C}). The subscript of these symbols indicates the buckling mode: l is local buckling and d is distortional buckling. The superscript of these symbols indicates the boundary condition. The abscissas in the figures show the half-wavelength for SCs and actual length for BCs, and they are presented in the form of a logarithmic scale and are all ranged from 30*mm* to 4000*mm*. From these figures, few findings are summarised below:

(1) From the BCs, it can be observed that with length increases, the three rack sections experience the L, SD (symmetric distortional), AD (antisymmetric distortional) + TF, and TF buckling. Under the $S-S$ boundary condition, the L + D buckling is observed only on the ZA30 section (see Fig. 6(a)). The L + D buckling is observed on the ZA30 and ZA32 sections under the $C-C$ boundary condition (see Fig. 6(b) and 7(b)). L + D buckling regions are located between the L and SD regions and are very narrow (widths ≤ 20*mm*), and there is no evidence of showing that the interactive buckling modes affected the buckling loads.

(2) The appearing of AD modes of the three rack sections is always accompanied by TF mode. At the lengths where the sections experiencing AD + TF buckling, the buckling loads are lower than the sections experiencing pure TF buckling; see the gap between the BC and the TF-FSM curve in each figure. With the increase in length, the participation of the AD modes decreased. The buckling modes, therefore, approach pure TF modes and hence the gaps close gradually.

(3) The critical buckling half-wavelengths and critical buckling loads of the three rack sections are indicated in the figures and are listed in Table 6. The SCs in Fig. 8 fails to show the (l_{crd}^{S-S}, P_{crd}^{S-S}) and (l_{crd}^{C-C}, P_{crd}^{C-C}) of the ZA42 section; consequently, they were determined using the methodology of $FSM@cFSM-l_{cr}$ [23].

(4) For the BCs ($C-C$ boundary condition) of the three rack sections, the buckling loads gradually decrease after the lengths of their l_{crl}^{C-C} and approach their P_{crl}^{S-S}; see the BCs in Fig. 6(b), Fig. 7(b), and Fig. 8(b). Hancock [25] pointed out that when multiple local or

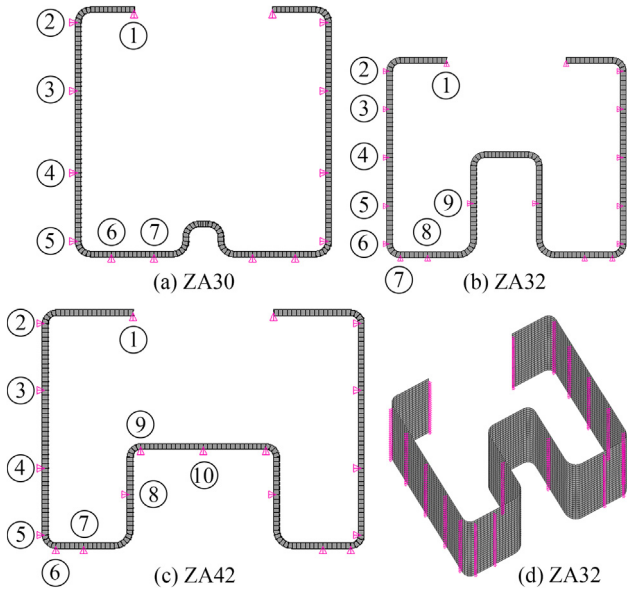

Fig. 5. Selected nodal lines in the FEM models.

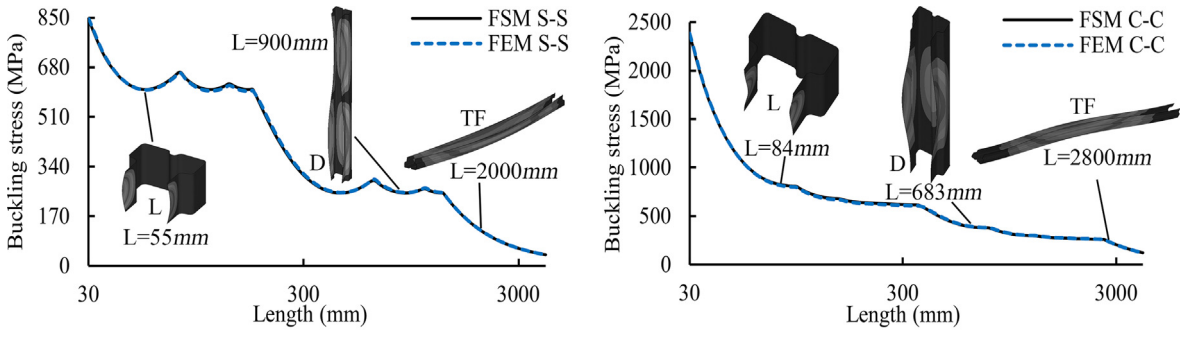

(a) under the S-S boundary condition (b) under the C-C boundary condition

Fig. 4. Buckling curves of specimen D1.

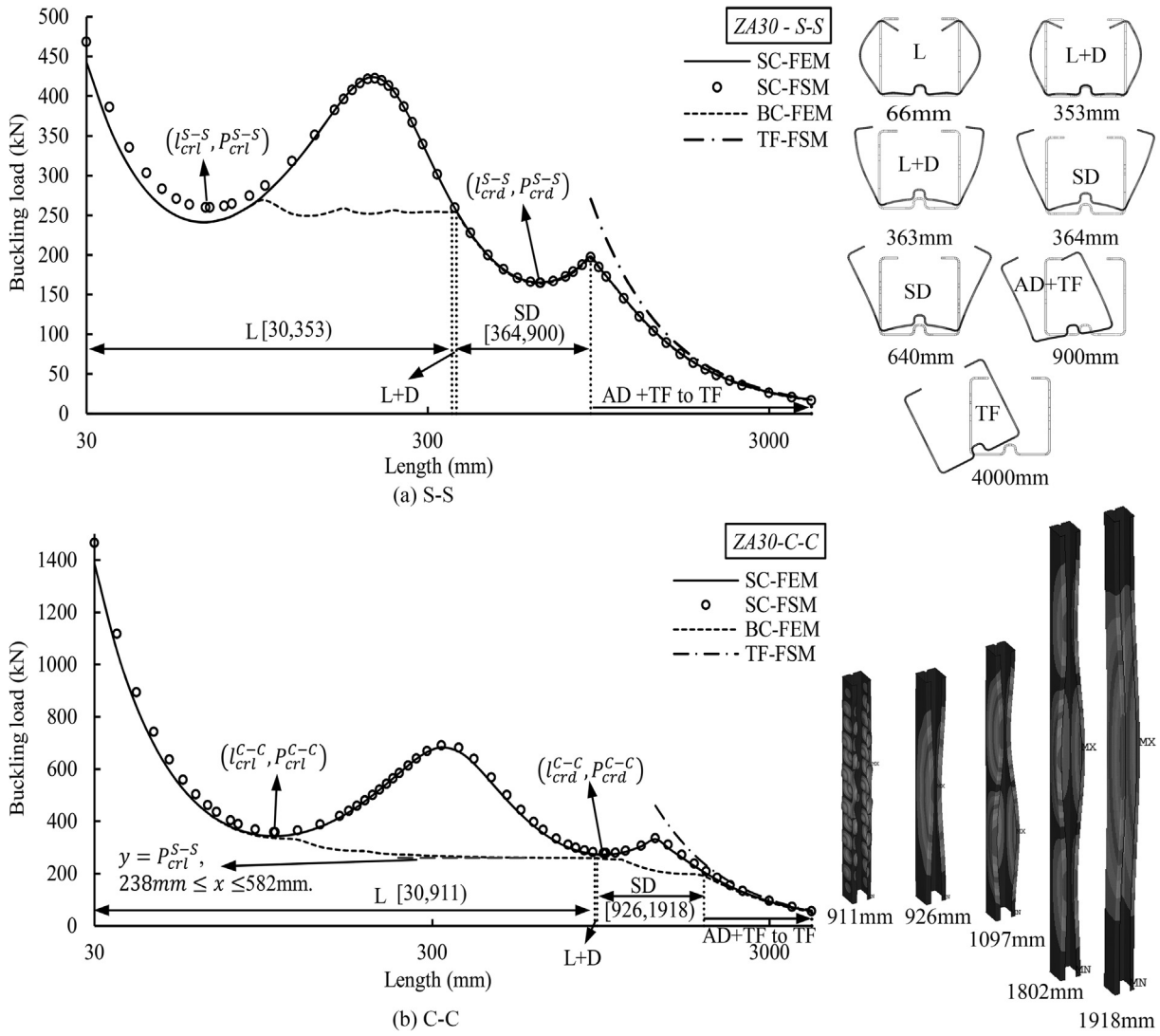

Fig. 6. Signature curves and buckling curves of the solid ZA30 section.

distortional buckling half-wavelengths occur in a column under compression, the effect of end boundary conditions on the buckling load is diminished. This phenomenon is termed here as the multi-half-wavelengths effect.

(5) While experimentally determining the local buckling capacity of rack columns, the AISI S902 [26] requires the specimen lengths shall not be less than three times the greatest width of the cross-section and not exceed 20 times the minimum radius of gyration (r). This length range is presented in Fig. 6(b), Fig. 7(b), and Fig. 8(b) by the blue and dashed lines, and the lines have a uniform ordinate of the corresponding P_{crl}^{S-S}. Since the local buckling of the three rack sections all occurred at flanges, the width of flanges (F) is used here instead of the greatest width of the cross-sections. From Fig. 6(b), Fig. 7(b), and Fig. 8(b) it can be observed that when the $L = 3F$, the ZA30, ZA32, and ZA42 sections have the buckling loads are 5.0%, 5.5%, and 6.6% above their P_{crl}^{S-S}, respectively. Although the differences are not significant, the longer the lengths, the smaller the differences.

(6) In practice, rack columns are usually braced continuously along the length, which allows for the occurrence of multiple buckling half-wavelengths. In the DSM [1], for considering the multi-half-wavelengths effect, a column piece between adjacent two bracings is isolated and assumed to be under the $S - S$ boundary condition. The P_{crl}^{S-S}, P_{crd}^{S-S}, and global buckling loads are the input parameters of the DSM, and this is why the SC is deemed an indispensable tool for designing rack columns. From Fig. 6(b), Fig. 7(b), and Fig. 8(b), it can be observed that the $(l_{crl}^{S-S}, P_{crl}^{S-S})$ and $(l_{crd}^{S-S}, P_{crd}^{S-S})$ are not only shown in SCs but also shown in BCs, and the BCs coincide with the SCs at the global buckling regions. It is noted here that the P_{crd}^{S-S} of the three rack sections are smaller than their P_{crl}^{S-S}, which resulted in those distinct minima of the $(l_{crd}^{S-S}, P_{crd}^{S-S})$ to be shown in the BCs.

(7) In all the figures, the SCs from FEM coincide well with the SCs from FSM in the regions of distortional and global buckling, and the relative differences between the FEM results and the FSM results are within ± 5%. In local buckling regions, the SCs (FEM) shift downwards slightly from the SCs (FSM). For the SCs under the $S - S$ boundary condition, the shifts were due to the warping component caused by the end deformation was considered in the FEM models rather than the FSM models. The FSM overestimated the local buckling loads of rack sections under the $C - C$ boundary condition, which caused the shifts of the SCs (FEM). The critical buckling loads and critical buckling half-wavelengths of the three rack sections are given in Table 6 where the results captured from the SCs (FEM) were compared with those determined from the SCs (FSM). From Table 6, regarding the critical local buckling loads and critical local buckling half-wavelengths, it can be observed that the FEM results are lower than the FSM results by the relative differences of −2.1% to −7.1% and −2.4% to −4.3%, respectively. In terms of

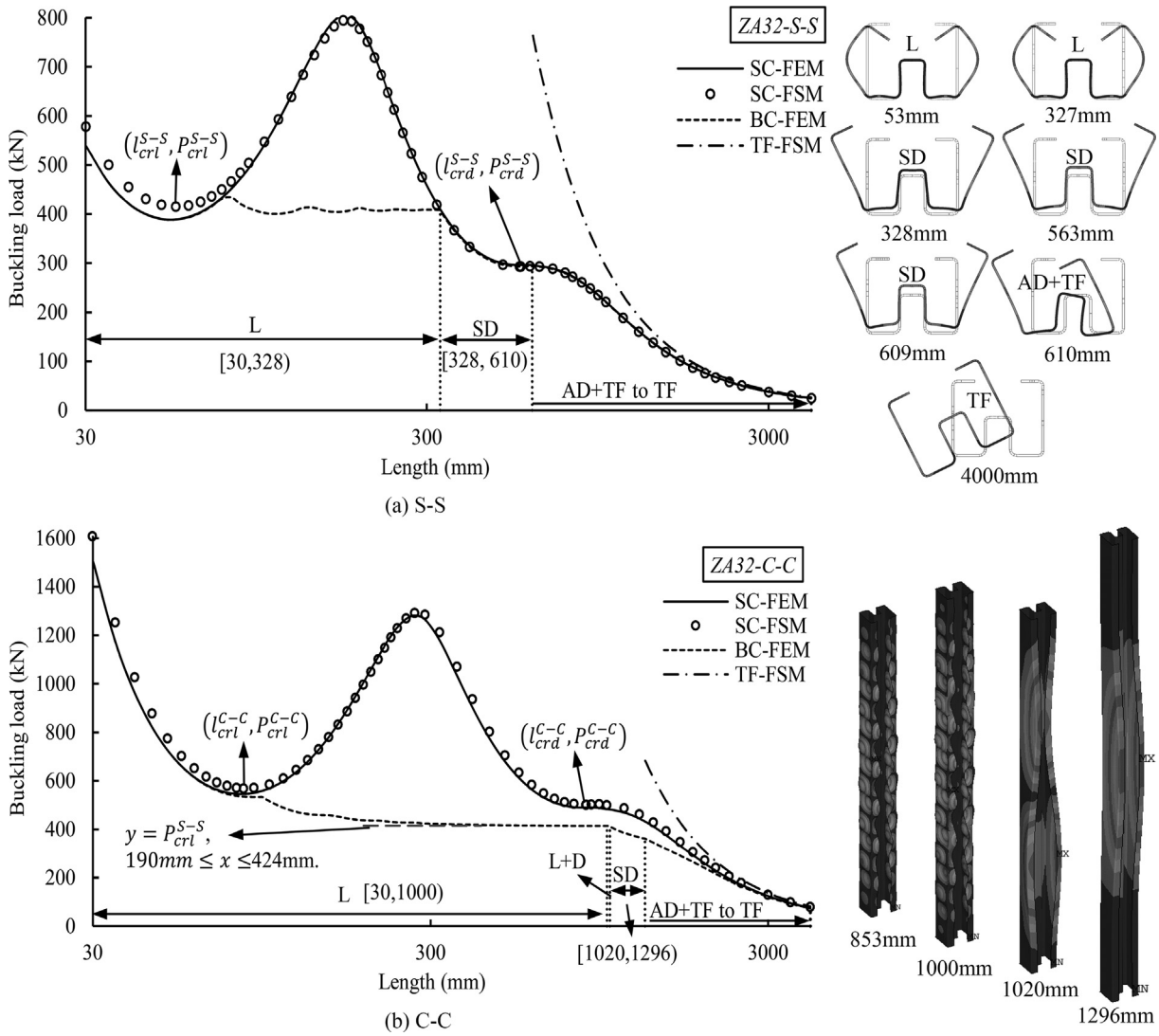

Fig. 7. Signature curves and buckling curves of the solid ZA32 section.

critical distortional buckling loads and critical distortional buckling half-wavelengths, the FEM results are very close to the FSM results by the relative differences of -2.5% to 1.0% and -1.7% to 0.0%, respectively. The critical buckling loads and critical buckling half-wavelengths captured from the BCs (FEM) are almost the same with those determined from the SCs (FEM), which are also presented in Table 6.

(8) The width and initial length of the buckling regions of the rack sections are apparently different under the two boundary conditions. For the BCs (under the $C-C$ boundary condition), the widths of local buckling regions are more than two times of those of the BCs (under the $S-S$ boundary condition). Moreover, the columns (under the $S-S$ boundary condition) showed a single distortional buckling half-wavelength while the columns (under the $C-C$ boundary condition) showed multiple distortional buckling half-wavelengths.

(9) The SCs (FEM and FSM) (under the $C-C$ boundary condition) fail to characterize the buckling behaviour of the rack sections. Firstly, the SCs fail to indicate the minimum local buckling load of the rack sections. Secondly, the SCs fail to show the distortional buckling regions and the minimum distortional buckling loads. Moreover, the SCs fail to present the initial length of the global buckling regions and even overestimate the buckling load of the ZA32 and ZA42 sections at the beginning of their global buckling regions.

4.3. Multi-half-wavelengths method

The effect of multi-half-wavelengths can be utilized to determine the $(l_{crl}^{S-S}, P_{crl}^{S-S})$ and $(l_{crd}^{S-S}, P_{crd}^{S-S})$ of rack sections. The way is to perform eigenbuckling analyses of a section under the $C-C$ boundary condition, and the models have the lengths of ml and are constrained or braced at the ends of each buckling half-wavelength. By doing this, fixed buckling half-wavelengths can be defined, and the interactions of local or distortional buckling with higher order buckling modes are prevented. The m is the number of buckling half-wavelengths; the l is the half-wavelength. Eigenbuckling analyses are performed by gradually changing the l; hence, a buckling curve can be generated. The minimum point in the buckling curve shows the critical buckling half-wavelength and critical buckling load. Two types of FE models can be adopted here. Type 1 model is the column model constrained by using Eq. (5). Odd numbers are defined for the m; hence, master nodes can be assigned to the cross-sections at the length centre. Type 2 model is the column models with its out-of-plane displacement of a few nodes restrained. The nodes are at the cross-sections of $Z = nl(n = 1, 2, 3, \cdots m-1)$, and their locations are shown in Fig. 5. The reason for proposing the two types of models is while for determining the $(l_{crd}^{S-S}, P_{crd}^{S-S})$, the type 2 model is only applicable to sections with their P_{crd}^{S-S} smaller than the P_{crl}^{S-S}.

The m should be large enough to fully diminish the restraint effect

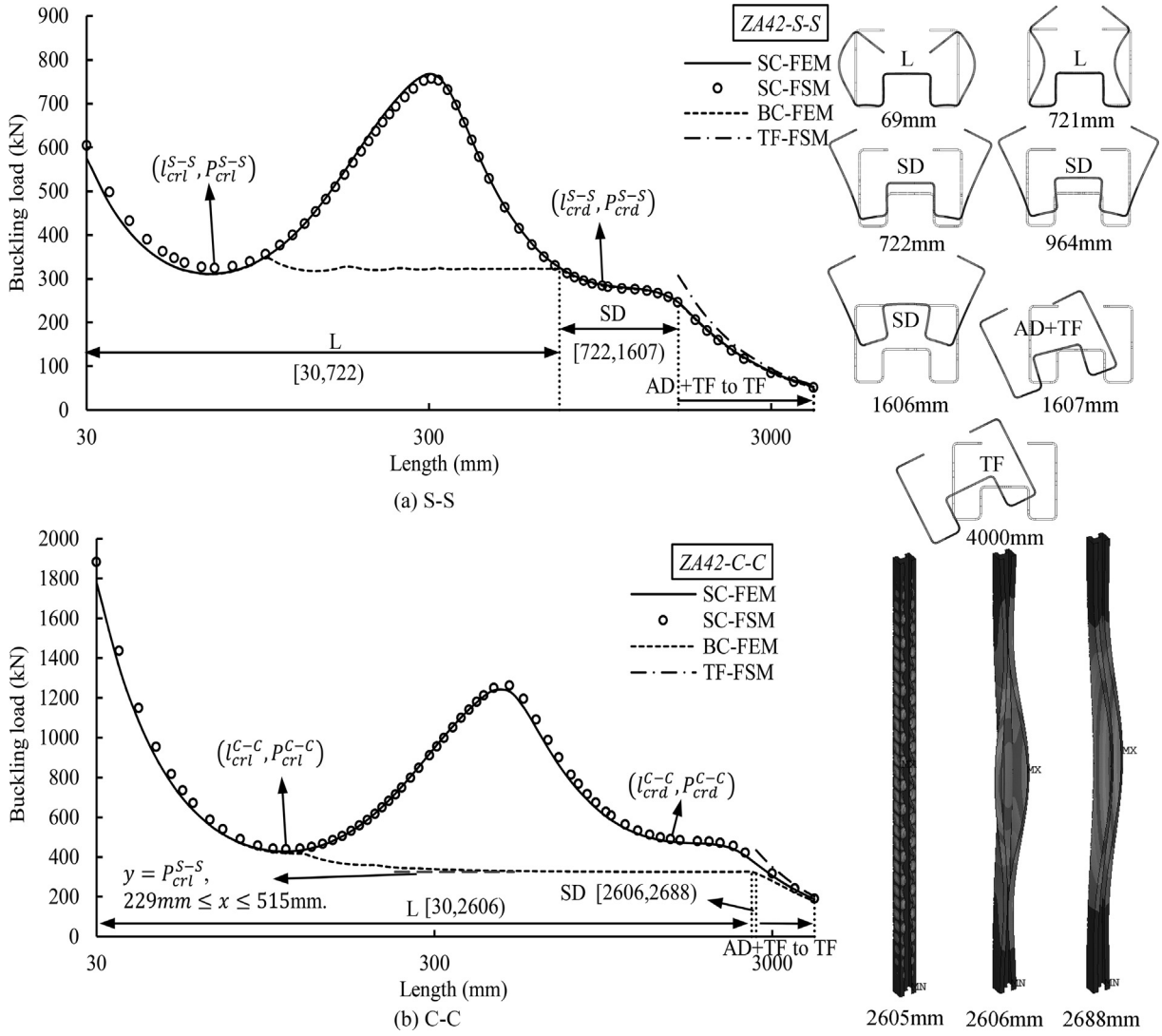

Fig. 8. Signature curves and buckling curves of the solid ZA42 section.

Table 6
Critical buckling loads and critical buckling half-wavelengths.

Parameters			ZA30		ZA32		ZA42	
			$S-S$	$C-C$	$S-S$	$C-C$	$S-S$	$C-C$
P_{crl} (kN)	FSM		259.8	358.7	415.0	567.6	325.6	437.1
	FEM	SC	241.3	343.2	388.4	545.8	311.4	427.8
		D (%)	−7.1	−4.3	−6.4	−3.8	−4.4	−2.1
		BC	241.2	–	388.1	–	311.0	–
		D (%)	−7.1	–	−6.5	–	−4.5	–
l_{crl} (mm)	FSM		69.0	105.0	55.0	85.0	71.0	110.0
	FEM	SC	66.0	102.0	53.0	83.0	69.0	107.0
		D (%)	−4.3	−2.9	−3.6	−2.4	−2.8	−2.7
		BC	66.0	–	53.0	–	69.0	–
		D (%)	−4.3	–	−3.6	–	−2.8	–
P_{crd} (kN)	FSM		164.9	277.8	292.8	500.8	284.2	491.3
	FEM	SC	165.3	272.2	295.6	489.8	286.2	479.0
		D (%)	0.3	−2.0	1.0	−2.2	0.7	−2.5
		BC	164.1	–	292.9	–	283.9	–
		D (%)	−0.5	–	0.0	–	−0.1	–
l_{crd} (mm)	FSM		641.0	983.0	563.0	868.0	964.0	1470.0
	FEM	SC	641.0	968.0	561.0	853.0	–	–
		D (%)	0.0	−1.5	−0.4	−1.7	–	–
		BC	640.0	–	563.0	–	–	–
		D (%)	−0.2	–	0.0	–	–	–

of the $C-C$ boundary condition. Sensitivity analyses of the m on the buckling loads of the rack sections were performed. The l_{crl}^{S-S} and l_{crd}^{S-S} were selected for the l, respectively, and both the type 1 and type 2 models were employed. The results yielded by the two types of models were close; hence, only the results of the type 2 models are presented in Fig. 9. It can be observed from the figure that when m reached 11, the ratios of P/P_{crl}^{S-S} and P/P_{crd}^{S-S} are very close to unity. One result of the ZA42 section is not shown in Fig. 9(b) since this column showed the local buckling when $m = 3$.

$$u_s = \sin(m\pi Z_s/L)\sin(\pi Z_s/L) \tag{5}$$

$$m = 2n + 1,\ n = 1, 2, 3, \cdots$$

The accuracy of using the multi-half-wavelengths method to determine the l_{crl}^{S-S} and l_{crd}^{S-S} of the rack sections was evaluated. The buckling curves generated by the two types of models are presented in Fig. 10. From Fig. 10(a), (c), and (e), it can be seen that the $(l_{crl}^{S-S}, P_{crl}^{S-S})$ shown here are almost the same as those FSM results (see Table 6). From Fig. 10(b), (d), and (f), it can be seen that the results of the type 1 models show the maximum differences of 3.9% and −2.3% on the l_{crd}^{S-S} and P_{crd}^{S-S}, respectively while compared with those FSM results in Table 6. In the case of the type 2 models, the maximum differences are 1.2% on the l_{crd}^{S-S} and 1.8% on the P_{crd}^{S-S}. In Fig. 10(f), the buckling curves fail to show the $(l_{crd}^{S-S}, P_{crd}^{S-S})$ of the ZA42 section, which agreed well with the SC (FSM) in Fig. 8(a).

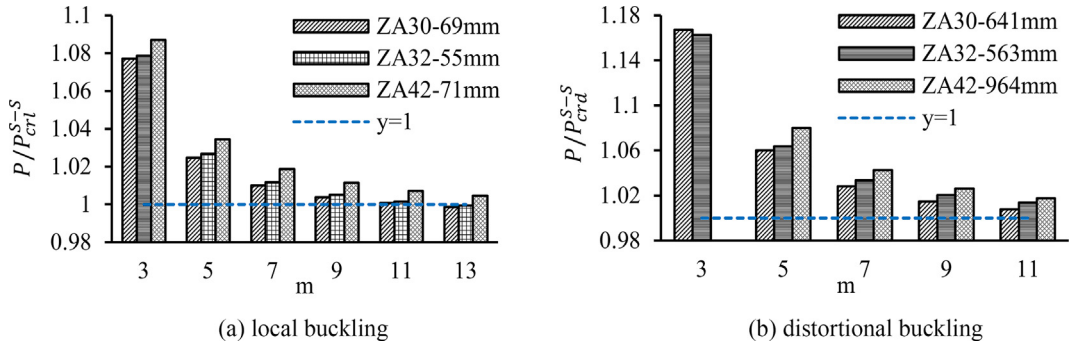

Fig. 9. Sensitivity of buckling loads on the number of buckling half-wavelengths.

5. Buckling behaviour of perforated rack sections

In this section, the buckling behaviour of the three rack sections with patterned holes was studied.

5.1. Perforation patterns effects

When cutting a piece from a rack column with patterned holes uniformly distributed along the length, the holes contained in that piece can be different. For generating the SCs and BCs of a perforated rack section, at each half-wavelength or length, the lowest buckling load among the buckling loads of all the possible perforation patterns should be selected. Sensitivity analyses of buckling loads of the three perforated rack sections on perforation patterns were performed here. Two strategies were proposed to do these analyses. Strategy 1 is illustrated in Fig. 11, and the column shown in this figure has the perforated ZA32 section and the length of $90mm$. For this perforation pattern sensitivity analysis, 33 numerical models were generated.

It will be time-consuming to use this strategy in the generations of SCs and BCs of the rack sections; hence, a simplified strategy (strategy 2) is proposed. For strategy 2, only five perforation patterns (perforation patterns (a) to (e)) are considered for rack sections with lengths experiencing local buckling. For rack sections with lengths experiencing distortional and global buckling, perforation patterns (b) to (e) are considered. The perforation patterns (a) to (e) are described below and examples are given in Fig. 12:

(1) Perforation pattern (a) (Fig. 12(c)) is a pair of flange holes opened at the centre of the column.
(2) Perforation pattern (b) (Fig. 12(e)) is a pair of web holes opened at the centre of the column.
(3) Perforation pattern (c) (Fig. 12(d)) is a pair of web holes opened at the top end of the column.
(4) Perforation pattern (d) (Fig. 12(a)) is a pair of web holes opened at the bottom end of the column.
(5) Perforation pattern (e) (Fig. 12(b)) is the column end opened by web holes with the same depth of openings.

For each perforated rack section, two lengths were randomly selected for the local, distortional, and global buckling (one for AD + TF buckling and one for TF buckling). Strategy 1 was used for performing the perforation pattern sensitivity analyses, and the ratios of the buckling load to the minimum buckling load (P/P_{min}) are plotted against the shift distance in Fig. 13. From Fig. 13(a) and (d), it can be seen that

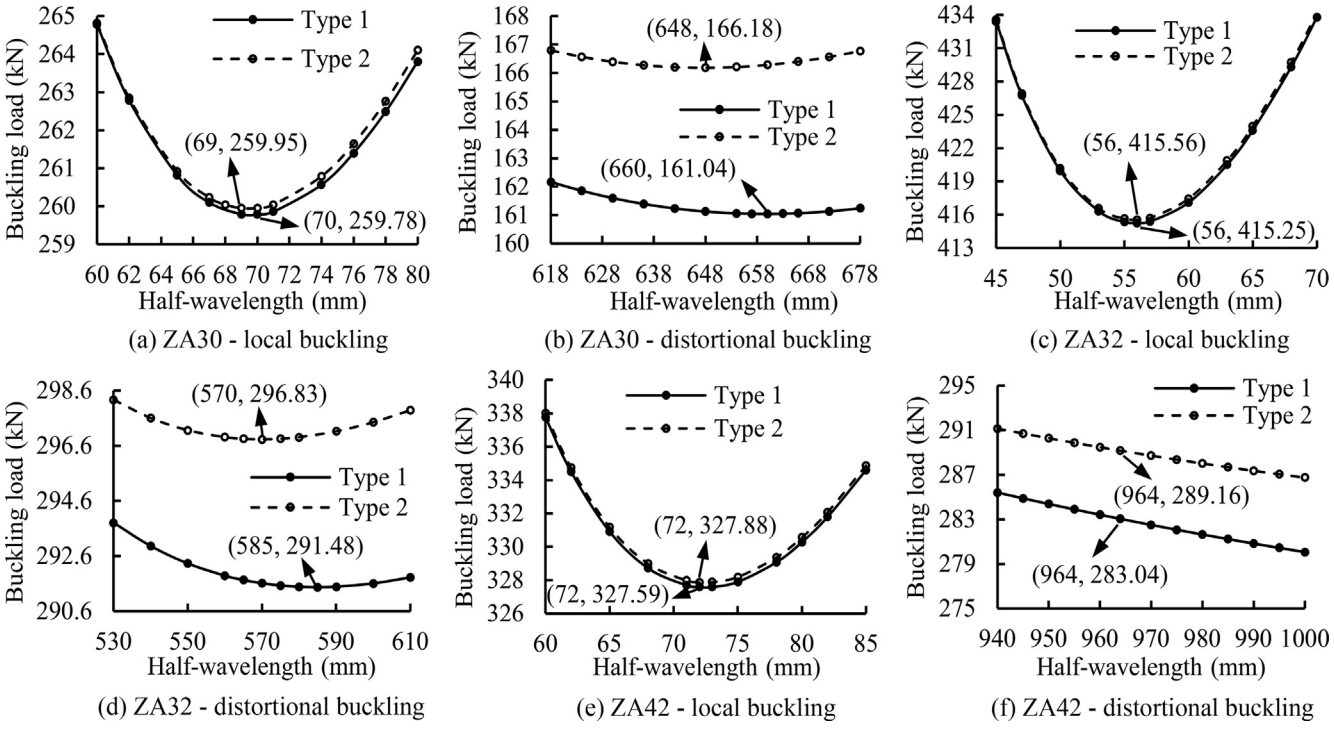

Fig. 10. Buckling curves generated by using the type 1 and type 2 models.

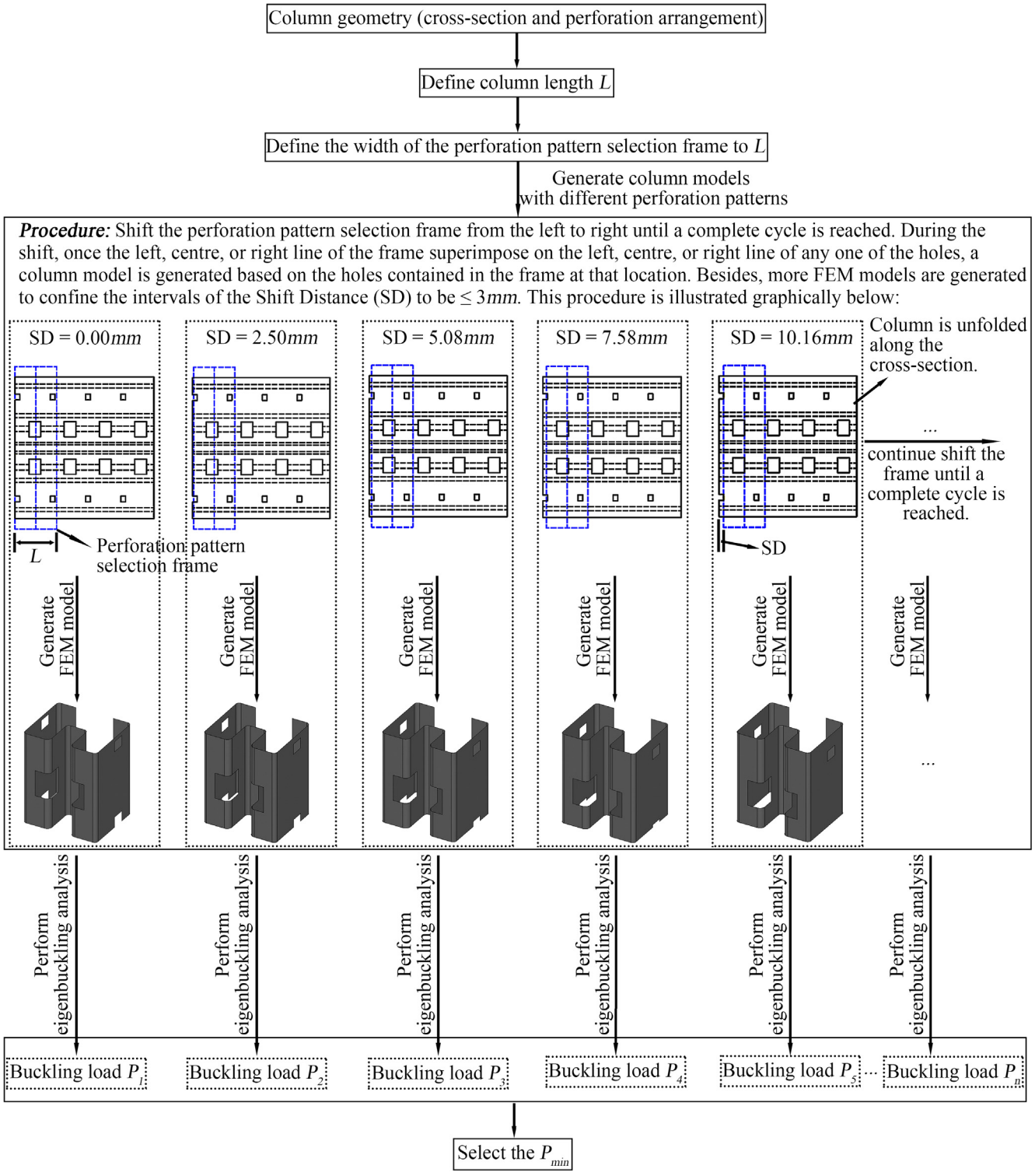

Fig. 11. Flowchart of strategy 1.

the maximum values of the P/P_{min} are 1.11, 1.15, and 1.08 for the ZA30, ZA32, and ZA42 sections with lengths experiencing local buckling, respectively. For the rack sections with lengths experiencing distortional buckling, the values of the P/P_{min} are all under 1.02 (see Fig. 13(b) and (e)). In global buckling cases, see Fig. 13(c) and (f), the values of the P/P_{min} are all less than 1.01. The local buckling loads are much more sensitive to perforation patterns than distortional and global buckling loads.

The performance of strategy 2 was evaluated. The yielded results of the perforation pattern sensitivity analyses by using the two strategies are presented in Table 7. It can be seen from Table 7 that the buckling loads yielded by the two strategies are almost the same, and the relative differences are no more than 0.3%. The perforation patterns yielded the minimum buckling loads in strategy 2 are given in the sixth column of Table 7. It is interesting to find that in the local buckling cases, all the minimum buckling loads are obtained at the perforation pattern (a). This indicates that the flange holes opened at the peak of buckling halfwaves has the most significant effect on the columns' local buckling

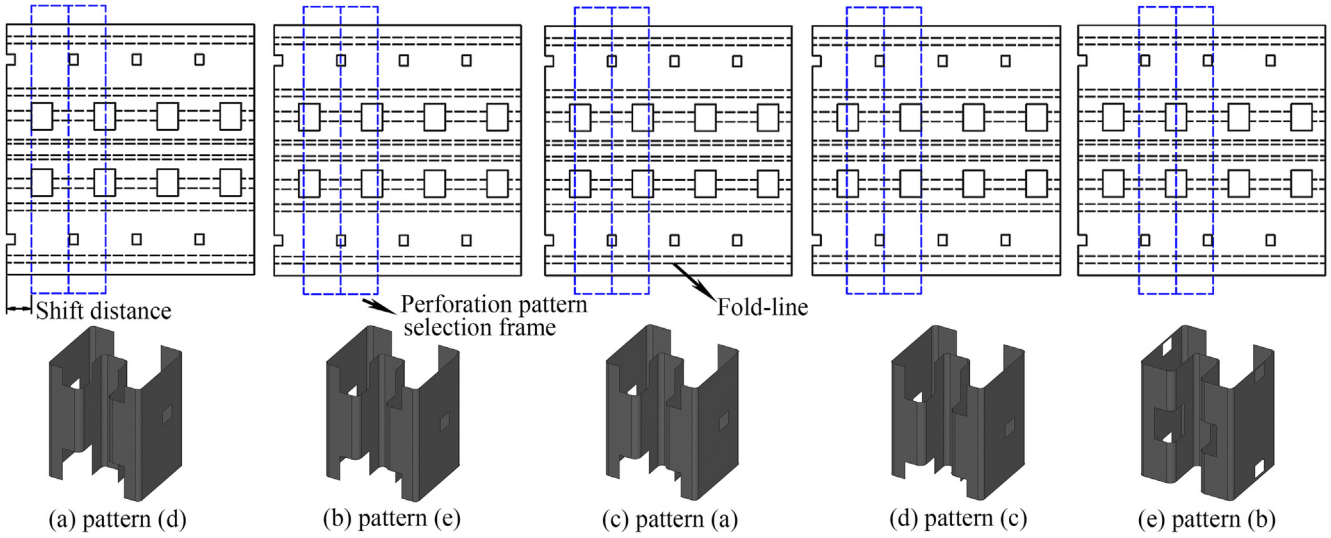

Fig. 12. Perforation patterns of the ZA32 column.

loads. It is proved here that strategy 2 is unbiased and accurate for performing the perforation pattern sensitivity analysis; hence, it is employed in the generations of SCs and BCs of the three perforated rack sections.

5.2. SCs and BCs of perforated rack sections

The BCs (under the $C-C$ boundary condition) of the three perforated rack sections were generated using the ANSYS 18.1 [22]. It is assumed that the shape function (Eq. (4)) of solid rack columns applies to perforated rack columns, and the SCs (under the $C-C$ boundary condition) of the perforated rack sections were generated as well. Strategy 2 was employed here for conducting the perforation pattern sensitivity analysis while one change was made: only the perforation pattern (b) was considered for the rack sections with lengths experiencing global buckling. The reason for making this change is it has been proved that the global buckling loads of the three rack sections are not sensitive to perforation patterns. It is found that the perforation pattern (the one yields the minimum buckling load) of the rack columns can be different from that of the same columns but with different constraints applied on them. As a result, the perforation pattern sensitivity analysis was performed in the generations of the SCs and BCs of the rack sections, individually.

The SCs and BCs of the three perforated rack sections are shown in Figs. 14–16. For the BCs: (1) the column buckling modes are indicated in the figures; (2) the boundaries between adjacent two different buckling modes are presented; and (3) few column buckling modes are selected and shown in the right side of the figures. The SCs and BCs shown here were compared with those of the solid rack sections under the $C-C$ boundary condition, and the influences of the holes on the

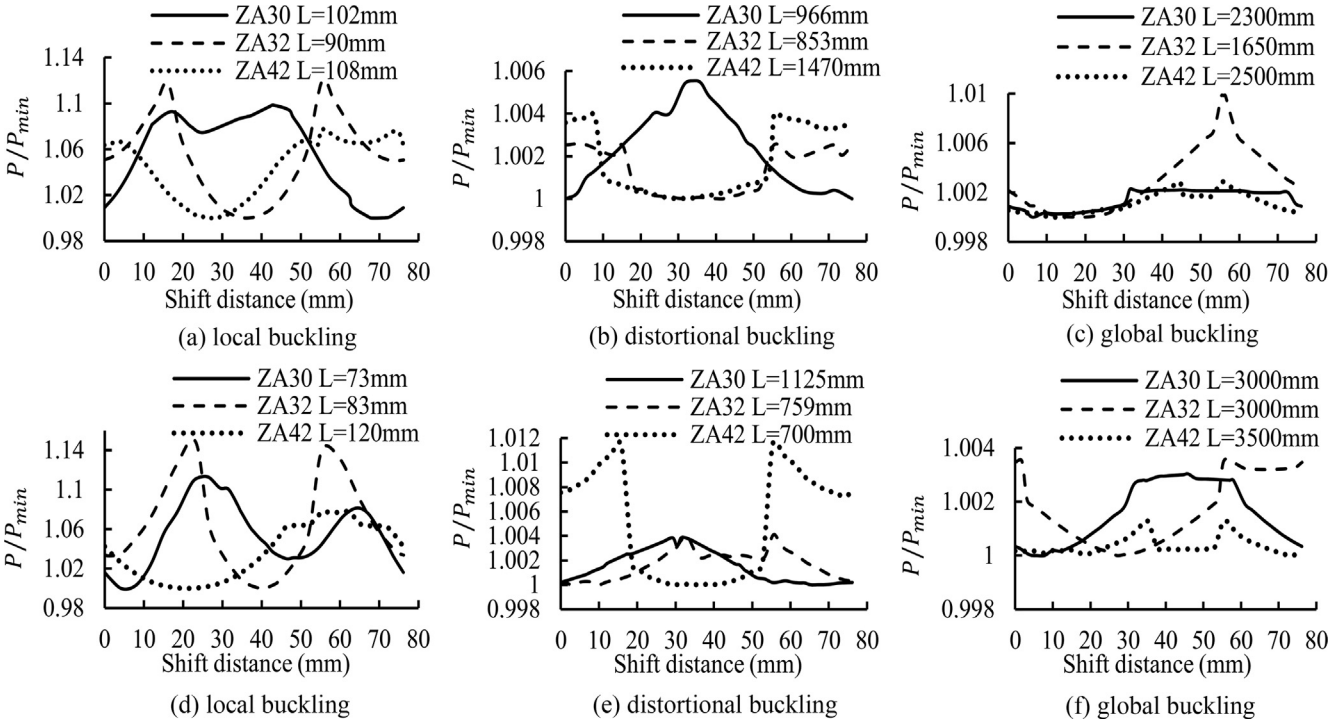

Fig. 13. Perforation pattern effects on columns' buckling loads.

Table 7
Perforation pattern sensitivity analyses results.

Buckling mode	Column	Length (*mm*)	Strategy 1	Strategy 2		Difference (%)
			$P(kN)$	$P(kN)$	Perforation pattern	
Local	ZA30	102	288.44	–	(a)	–
		73	339.48		(a)	
	ZA32	90	413.48		(a)	
		83	418.11		(a)	
	ZA42	108	341.39		(a)	
		120	339.62		(a)	
Distortional	ZA30	966	211.74	211.82	(b)	0.04
		1125	207.18	207.18	(b)	0.00
	ZA32	853	322.97	–	(c)	–
		759	334.37	335.14	(b) & (e)	0.23
	ZA42	1470	371.10	–	(d)	–
		700	671.43	671.43	(e)	0.00
Global	ZA30	2300	124.04	124.08	(d)	0.03
		3000	78.35	78.36	(d)	0.02
	ZA32	1650	211.45	211.65	(c)	0.09
		3000	87.19	–	(c)	–
	ZA42	2500	253.25	–	(b)	–
		3500	158.86	158.90	(b) & (e)	0.02

Note: '-' means the results yielded by strategy 2 are the same as those yielded by strategy 1; () & () means two perforation patterns occurred in a model simultaneously.

buckling modes and buckling loads are discussed below:

(1) The distortional buckling of the perforated rack sections takes place at relatively shorter lengths compared to those of the corresponding solid rack sections. The lengths start to show distortional buckling are 926*mm*, 1020*mm*, and 2606*mm* for the solid ZA30, ZA32, and ZA42 sections, respectively. The perforated rack sections start to show distortional buckling at the length of 820*mm* for the ZA30 section, 711*mm* for the ZA32 section, and 2198*mm* for the ZA42 section. Moreover, the widths of the distortional buckling regions are increased by the holes from 992*mm* to 1149*mm* (15.8% increment) for the ZA30 section, from 276*mm* to 624*mm* (126.1% increment) for the ZA32 section, and from 82*mm* to 211*mm* (157.3% increment) for the ZA42 section.
(2) The initial lengths of global buckling regions were postponed by the holes from 1918*mm* to 1969*mm* for the ZA30 section and from 1296*mm* to 1335*mm* for the ZA32 section. On the contrary, the perforated ZA42 section shows the global buckling firstly at the length of 2409*mm*, which is 279*mm* shorter than that of the solid ZA42 section (2688*mm*).
(3) The length ranges (x) of $[3F, 20r]$ are presented in Figs. 14–16 with uniform ordinates of the P_{crl}^{S-S} of the corresponding perforated rack sections. The determinations of the P_{crl}^{S-S} of the perforated rack sections are illustrated in Section 5.4. At the lengths of $3F$, the buckling loads of the perforated ZA30, ZA32, and ZA42 sections are 5.7%, 3.3%, and 8.1% above their P_{crl}^{S-S}, respectively.
(4) The SCs fail to characterize the buckling behaviour of the three perforated rack sections under the $C-C$ boundary condition (see the gap between the SC and BC in Figs. 14–16). This is similar to what has been found on the solid rack sections while the SCs here do not coincide with the BCs even at the lengths before the first minimum of the SCs. By checking the buckling modes (without constraint equation applied), it is observed that the buckling shapes of the perforated rack columns are not following the shape of the sinusoidal curve (Eq. (4)) in the longitudinal direction.

The buckling loads of the perforated rack sections yielded from the perforation pattern sensitivity analyses while generating the BCs are analyzed here. The ratios of the maximum buckling load to the minimum buckling load (P_{max}/P_{min}) are plotted against the ratios of the l/l_{crl}^{S-S} in Fig. 17. It can be observed from the figure that the ratios of the P_{max}/P_{min} become less than 1.01 when the ratios of the l/l_{crl}^{S-S} go beyond the 3.8, 3.6, and 4.7 for the ZA30, ZA32, and ZA42 sections, respectively. The shortest specimen length required in the AISI S902 [26] for determining the local buckling capacity of rack columns is $3F$. However, from the current study, it is observed that if the length is changed to $5l_{crl}^{S-S}$, the considerations of the effects of perforation pattern are not necessary and the yielded buckling loads are more conservative. The columns start to show distortional buckling after the ratios of the l/l_{crl}^{S-S} reached the 10.79, 12.26, and 28.55 for the ZA30, ZA32 and ZA42 sections, respectively. Beyond these lengths, the ratios of the P_{max}/P_{min} are very close to unity. This explains why only the pattern (b) was

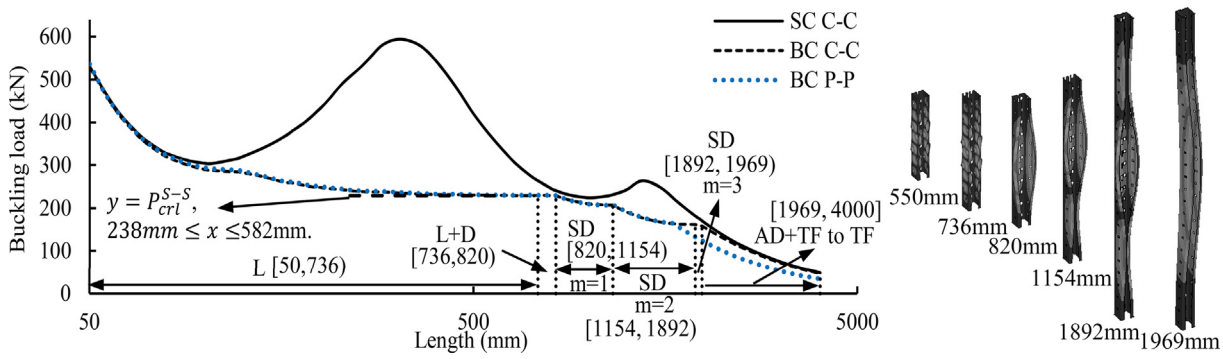

Fig. 14. Signature curve and buckling curves of the perforated ZA30 section.

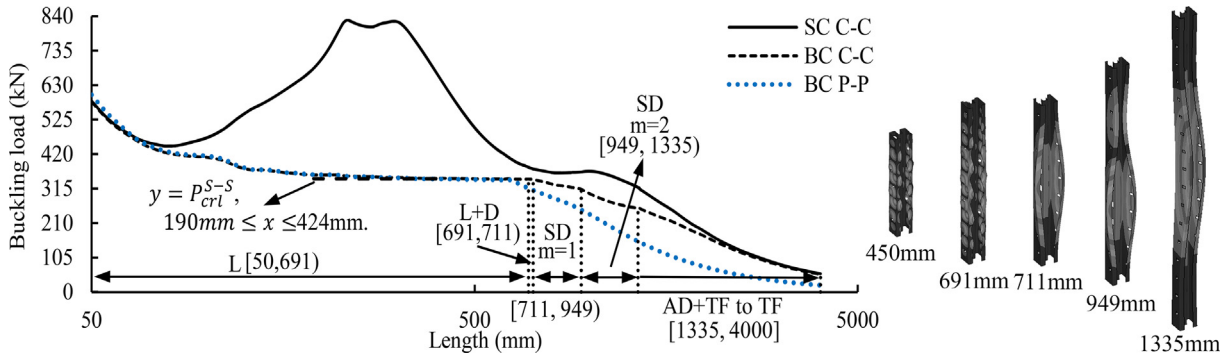

Fig. 15. Signature curve and buckling curves of the perforated ZA32 section.

considered for the global buckling cases while generating the SCs and BCs.

5.3. Columns under Pinned-Pinned boundary condition

It is difficult to test rack columns under the $S-S$ boundary condition experimentally; therefore, the boundary condition of Pinned-Pinned ($P-P$) is generally employed by scientists to determine the compression capacity of rack columns. The $P-P$ boundary condition is to restrain the cross-sectional deformation, torsion, and warping of a column's ends, but the column ends can rotate about the two principal axes of the cross-section. To date, however, scientists failed to justify the applications of the $P-P$ boundary condition in experiments since the erosion of the buckling load of rack columns due to the multi-half-wavelengths effect may not be properly considered.

Eigenbuckling analyses were performed to generate the BCs of the three perforated rack sections under the $P-P$ boundary condition. An FE model with the ZA42 section is shown in Fig. 18. In this figure, the column ends are rigidly attached to two steel loading plates, and the thickness of the loading plates is $30mm$. At the top face of each loading plate, there is a steel block at the centre. The depth of the steel blocks is $40mm$, and their centroids coincide with the effective centroid of the column. The effective centroid is a point on the cross-section of a rack column that the column can reach the maximum capacity when a concentrated compressive force applied on this point. The details of the determination of the effective centroid of the three perforated rack sections can be found in [21]. The Solid185 element was used for the loading plates and steel blocks, and the Shell63 element was used for the column. The column ends share the nodes with the loading plates at the two interfaces, and a layer of the Shell63 elements is assigned to each interface since the nodes of the Solid185 element have none of the rotational degrees of freedom, and hence, can not prevent the rotations of the nodes of the Shell63 element. The boundary condition $P-P$ is applied to the nodes at the top face of each steel block. The left end of the model is the loading end. At the loading end, a unit force ($F_z = 1\ kN$) is applied to the node at the centroid of the steel block (see the white arrow), and the U_x and U_y of this node are restrained. Another two nodes with their U_x having restrained are collinear with the loading node. The right end of the model is restrained likewise except the U_z of the node at the centroid of the steel block is restrained.

The BCs of the three perforated rack sections under the $P-P$ boundary condition are shown in Figs. 14–16, and the following findings are summarized:

(1) The BCs under the $P-P$ boundary condition coincide well with the BCs under the $C-C$ boundary condition from the very beginning, and then the two curves start to separate from the lengths of $1653mm$, $626mm$, and $1254mm$ for the perforated ZA30, ZA32, and ZA42 sections, respectively. After the separations, the BCs under the $P-P$ boundary condition drop fast. The sections under the $P-P$ boundary condition start to show different buckling modes, which are responsible for the separations. To be specific, at the length of $1653mm$, the perforated ZA30 section under the $C-C$ boundary condition is close to the end of its distortional buckling region while the section under the $P-P$ boundary condition starts to show the AD + TF buckling. At the length of $626mm$, the perforated ZA32 section under the $C-C$ boundary condition is close to the end of its local buckling region, whereas the section under the $P-P$ boundary condition starts to show the distortional buckling. The perforated ZA42 section under the $C-C$ boundary condition remains in the local buckling region at the length of $1254mm$ while the section under the $P-P$ boundary condition starts to show the SD + F buckling. For those rack sections under the $P-P$ boundary condition, the distortional buckling or global buckling occurrs at shorter lengths than those rack sections under the $C-C$ boundary condition.

(2) The global buckling modes of the perforated ZA32 and ZA42 sections under the $C-C$ boundary condition are AD + TF or TF buckling modes while the two rack sections showed the SD + F buckling mode under the $P-P$ boundary condition.

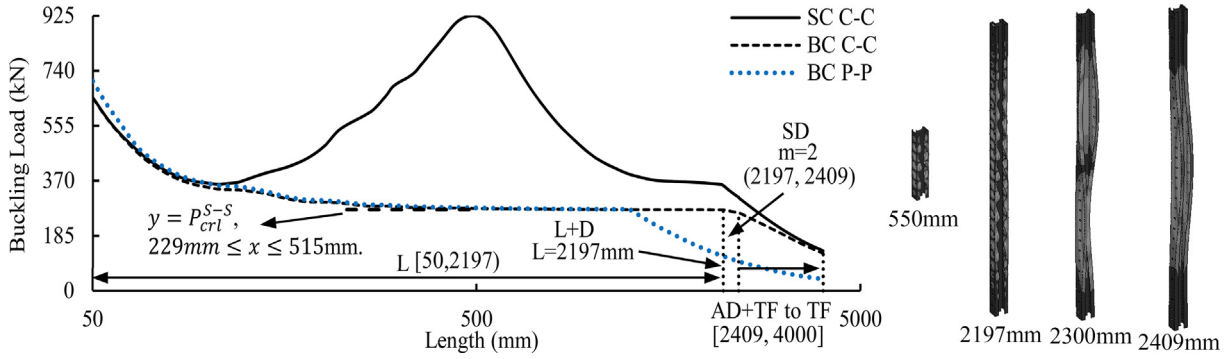

Fig. 16. Signature curve and buckling curves of the perforated ZA42 section.

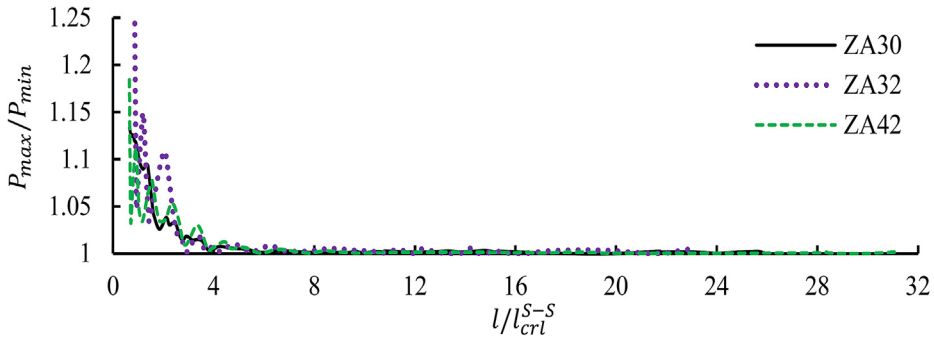

Fig. 17. The ratios of the maximum buckling loads to the minimum buckling loads.

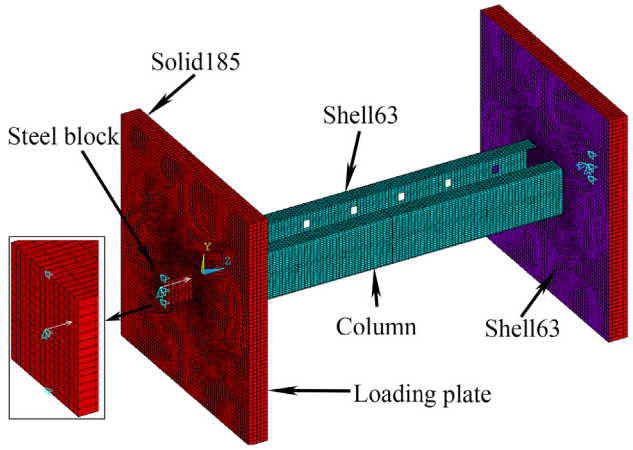

Fig. 18. A FEM model with the perforated ZA42 section under pinned–pinned boundary condition.

(3) The probable estimation of the critical distortional buckling load (P_{crd}^{S-S}) of a rack section using the $P-P$ boundary condition is checked here. Two methods were proposed, and their performances were evaluated. The first method is to perform an eigenbuckling analysis on a rack section under compression, and the rack section has the length two times its critical distortional buckling half-wavelength ($2l_{crd}^{S-S}$) and is under the $P-P$ boundary condition. The buckling load of the first buckling mode serves as an estimation of the P_{crd}^{S-S}. The determinations of the (l_{crd}^{S-S}, P_{crd}^{S-S}) of the three perforated rack sections are presented in Section 5.4. The second method is to use the buckling load of a rack section with the length at its end of the distortional buckling region as the estimation of the P_{crd}^{S-S}. The results (buckling load P and buckling mode) obtained from the two methods are presented in Table 8 where the ratios of P/P_{crd}^{S-S} are shown as well. It can be observed from the table that most of the ratios of the P/P_{crd}^{S-S} are far away from 1.0. There are two cases, not shown in Table 8, where the distortional buckling mode (SD) of the perforated ZA32 section under the $P-P$ boundary condition gradually transfers to the global buckling mode (SD + F) along the length, which made the end of the distortional buckling region very difficult to determine. For the perforated ZA42 section under the $P-P$ boundary condition, distortional buckling mode is not observed since the column presents global buckling (SD + F mode) right after the local buckling region. The two methods failed to provide accurate estimations of the P_{crd}^{S-S} of the rack sections; consequently, it can be concluded that the $P-P$ boundary condition is not suitable for determining the critical distortional buckling load of rack columns.

5.4. Determination of critical buckling loads

The SCs of the three perforated rack sections under the $S-S$ boundary condition were not generated since the results of trial simulations showed that along the length, the out-of-plane displacement of the columns' buckling modes failed to follow the shape of a single half-sinewave. The multi-half-wavelengths method (by using the type 2 models), consequently, was used here to determine the (l_{crl}^{S-S}, P_{crl}^{S-S}) and (l_{crd}^{S-S}, P_{crd}^{S-S}) of the three perforated rack sections, and the perforation pattern effects were considered. The results are presented in Table 9, and the buckling curves are shown in Fig. 19. It may be argued that like solid rack sections, the critical buckling loads and critical buckling half-wavelengths of perforated rack sections could be determined by generating their buckling curve under the $S-S$ boundary condition. This method could be more efficient to determine the critical buckling load compared to that of the multi-half-wavelengths method. The reason to use type 2 models is that the BCs (under the $S-S$ boundary condition) underestimated the (l_{crl}^{S-S}, P_{crl}^{S-S}) of the solid rack sections due to the influence of the warping of the loading end. Whereas, the $S-S$ boundary condition is proposed for solid thin-walled columns, which may not be applied to perforated rack columns.

The (l_{crl}^{S-S}, P_{crl}^{S-S}) and (l_{crd}^{S-S}, P_{crd}^{S-S}) of perforated rack sections were compared with those of solid rack sections, and the relative differences are presented in Table 9. The results show that after considering the holes, the critical local buckling loads are decreased by −11% to −17%. The critical distortional buckling loads are dropped more significantly than the critical local buckling loads where the decrements are −18.0%, −27.5%, and −23.1% for the ZA30, ZA32, and ZA42 sections, respectively. On the contrary, the critical local buckling half-wavelengths and critical distortional buckling half-wavelengths are increased due to the holes, and the increments are close to or less than 10%. In the case of the perforated ZA42 section, it was difficult to determine the (l_{crd}^{S-S}, P_{crd}^{S-S}). The P_{crd}^{S-S} of this section can be properly

Table 8
Estimations of the P_{crd}^{S-S} of the perforated rack sections using the $P-P$ boundary condition.

Column	Method 1				Method 2			
	Length (mm)	Buckling mode	$P(kN)$	P/P_{crd}^{S-S}	Length (mm)	Buckling mode	$P(kN)$	P/P_{crd}^{S-S}
ZA30	1362	SD	179.56	1.33	1652	SD	164.52	1.22
ZA32	1136	SD	198.83	0.94	–	–	–	–
ZA42	1928	SD + F	144.88	0.66	–	–	–	–

Table 9
Critical buckling loads and half-wavelengths of perforated rack sections.

Section	Buckling properties			
	$P_{crl}^{S-S}(kN)$	$l_{crl}^{S-S}(mm)$	$P_{crd}^{S-S}(kN)$	$l_{crd}^{S-S}(mm)$
ZA30	229.4	76.0	135.2	681.0
D (%)	−11.7	10.1	−18.0	6.2
ZA32	345.0	58.0	212.3	568.0
D (%)	−16.9	5.5	−27.5	0.9
ZA42	273.1	77.0	218.6*	964.0*
D (%)	−16.1	8.5	−23.1	0.0

Note:
* means the value is an estimation.

estimated using the buckling load of the perforated section at the l_{crd}^{S-S} of the solid ZA42 sections. This is because the holes do not significantly change the distortional buckling half-wavelengths of the ZA30 and ZA32 sections, whereas the buckling curve of the perforated ZA42 section is quite flat (see Fig. 19(f)).

6. Conclusion

This paper introduces the elastic buckling behaviour of the rack columns with three different Σ-shaped sections under uniaxial compression. Two scenarios were considered: the sections without holes and the sections with patterned holes distributed along the length uniformly. The buckling behaviour of the rack sections under these two scenarios was compared by generating their buckling curves. The ANSYS 18.1 [22] was successfully used for generating the signature curves of the three solid rack sections. The sensitivity analyses of perforation patterns on the buckling loads of local, distortional, and global buckling were performed, and the perforation pattern effects were well considered in the generations of the signature curves and buckling curves of the perforated rack sections. The critical buckling loads and critical buckling half-wavelengths of both the solid and perforated rack sections under the $S-S$ boundary condition were accurately determined using the multi-half-wavelengths method. The possibility of using the pinned-pinned boundary condition for estimating the critical distortional buckling load (under the $S-S$ boundary condition) was checked. The following conclusions are made from this study:

(1) The boundary conditions have significant effects on rack sections' buckling load, buckling mode, and the region of buckling modes. The pinned-pinned boundary condition is not suitable to determine the critical distortional buckling load (under the $S-S$ boundary condition) of rack sections.
(2) The multi-half-wavelengths effect should be properly considered in the experimental tests and structural design of rack columns. The pinned-pinned boundary condition should be used with caution for experimentally determining the distortional buckling capacity of rack columns under compression since it may not be able to properly consider the effect of multi-half-wavelengths.
(3) After considering the holes, the critical local buckling load and critical distortional buckling load of the three rack sections (under the $S-S$ boundary condition) are decreased by more than 10%. On the contrary, the critical local buckling half-wavelength and critical distortional buckling half-wavelength are increased, and the increments were close to or less than 10%.
(4) The multi-half-wavelengths method has been proved to be unbiased and accurate for determining the critical buckling loads and critical buckling half-wavelengths of perforated rack sections under the $S-S$ boundary condition, and the type 2 model and the number of buckling half-wavelengths of 11 are suggested.
(5) Signature curves (under the $C-C$ boundary condition) failed to characterize the buckling mode and buckling load of the rack sections under compression; hence, they are not suggested to be the references for predicting the compression capacity of rack columns under the $C-C$ boundary condition.
(6) Perforation pattern effects on the local buckling load of the three rack sections are significant when these columns have lengths less than five times the critical local buckling half-wavelength (l_{crl}^{S-S}). The effects on the distortional and global buckling loads of the three rack sections are minor and can be ignored.
(7) The trigonometric shape functions adopted in the finite strip

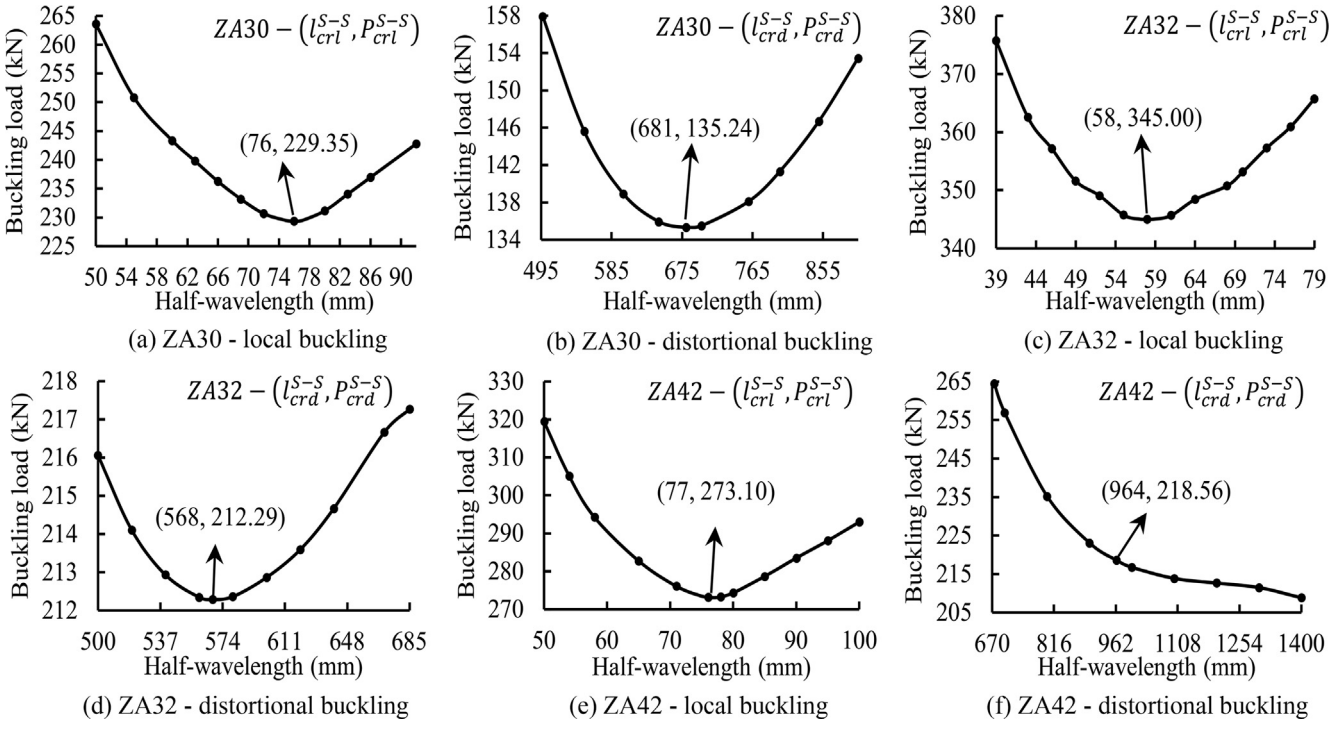

Fig. 19. Buckling curves of the three perforated rack sections.

method failed to describe the buckling shapes of perforated rack columns accurately and hence, should be avoided.

(8) To determine the local buckling capacity of a rack column experimentally, it is suggested here that the specimen lengths shall not be less than five times the critical local bucking half-wavelengths (l_{crl}^{S-S}) and not exceed 20 times the minimum radius of gyration (r).

Currently, the development of simplified methods for determining the critical elastic buckling properties of thin-walled perforated rack sections under compression are being pursued by scientists. The multi-half-wavelengths method is proposed in this paper, which can accurately determine the critical elastic buckling properties of Σ-shaped perforated rack sections under compression. This method can be a robust tool to be employed for validating the simplified methods. Future research will look into its applicability to other shapes of rack sections (e.g., channel and Ω). The results of this paper provide a strong basis for the design (the selection of input parameters), experimental tests (the selection of boundary conditions), and numerical simulations (the generation of robust numerical models) of both solid and perforated rack columns under compression. This paper, however, only focusses on the elastic buckling behaviour of rack columns under compression. Further research works are needed for developing guidelines on the selection of input parameters (elastic buckling properties) in analytical design solutions of rack columns under compression. Moreover, to facilitate the design of perforated rack columns, it is necessary to propose design formulas for determining critical elastic buckling properties of rack sections with various arrangements of opening patterns, dimensions, and spacing.

Declaration of Competing Interest

The authors declare that they have no known competing financial interests or personal relationships that could have appeared to influence the work reported in this paper.

Acknowledgements

Financial contributions of Natural Sciences and Engineering Research Council of Canada (NSERC) [Engage Grant], College of Graduate Studies of University of British Columbia [University Graduate Fellowship], and China Scholarship Council [CSC scholarship] were critical to conduct this study. The authors also acknowledge CMC Microsystems for the provision of products and services that facilitated this research, including ANSYS Multiphysics.

Appendix A. Supplementary material

Supplementary data to this article can be found online at https://doi.org/10.1016/j.engstruct.2020.110469.

References

[1] AISI_S100. North American Specification for the Design of Cold-Formed Steel Structural members. Washington, DC: American Iron and Steel Institute; 2016.
[2] Yang D, Hancock GJ. Compression tests of high strength steel channel columns with interaction between local and distortional buckling. J Struct Eng. 2004.
[3] Kwon YB, Kim BS, Hancock GJ. Compression tests of high strength cold-formed steel channels with buckling interaction. J Constr Steel Res. 2009;65:278–89.
[4] Casafont M, Pastor MM, Roure F, Peköz T. An experimental investigation of distortional buckling of steel storage rack columns. Thin Wall Struct. 2011;49:933–46.
[5] Dinis PB, Young B, Camotim D. Local–distortional interaction in cold-formed steel rack-section columns. Thin Wall Struct. 2014;81:185–94.
[6] Li ZB. Schafer Buckling analysis of cold-formed steel members with general boundary conditions using CUFSM: conventional and constrained finite strip methods. In: LaBoube RA, Yu W-W, editors. 20th Int Spec Conf on Cold-Formed Steel Structures. Missouri University of Science and Technology; 2010.
[7] Bebiano R, Camotim D, Gonçalves R. GBTul 2.0 − A second-generation code for the GBT-based buckling and vibration analysis of thin-walled members. Thin Wall Struct. 2018;124:235–57.
[8] Hancock GJ. Distortional buckling of steel storage rack columns. In: Yu W-W, Senne JH, editors. 7th Int Spec Conf on Cold-Formed Steel Structures. Department of Civil Engineering University of Missouri - Rolla; 1984. p. 345–73.
[9] Hancock GJ, Roos O. Flexural-torsional buckling of storage rack columns. In: Yu W-W, Senne JH, editors. 8th Int Spec Conf on Cold-Formed Steel Structures. Department of Civil Engineering University of Missouri - Rolla; 1986. p. 329–51.
[10] Davies JM, Leach P, Taylor A. The design of perforated cold-formed steel sections subject to axial load and bending. Thin Wall Struct. 1997;29:141–57.
[11] Casafont M, Pastor MM, Roure F, Bonada J, Peköz T. Design of steel storage rack columns via the direct strength method. J Struct Eng. 2012.
[12] Yao Z, Rasmussen KJ. Perforated Cold-Formed Steel Members in Compression. II: Design. J Struct Eng 2016.
[13] Moen C, Schafer B. Direct strength method for design of cold-formed steel columns with holes. J Struct Eng 2010.
[14] Pastor M, Bonada J, Roure F, Casafont M. Residual stresses and initial imperfections in non-linear analysis. Eng Struct 2013;46:493–507.
[15] Bonada J, Pastor M, Roure F, Casafont M. Influence of the cold work effects in perforated rack columns under pure compression load. Eng Struct 2015;97:130–9.
[16] Smith FH, Moen CD. Finite strip elastic buckling solutions for thin-walled metal columns with perforation patterns. Thin-walled Struct 2014;79:187–201.
[17] Zhao X, Ren C, Qin R. An experimental investigation into perforated and non-perforated steel storage rack uprights. Thin Wall Struct 2017;112:159–72.
[18] Trouncer A, Rasmussen K. Flexural–torsional buckling of ultra light-gauge steel storage rack uprights. Thin Wall Struct 2014;81:159–74.
[19] Crisan A, Ungureanu V, Dubina D. Behaviour of cold-formed steel perforated sections in compression. Part 1-Experimental investigations. Thin Wall Struct 2012;61:86–96.
[20] Casafont M, Roure F, Pastor M, Bonada J, Peköz T. Distortional buckling test for steel storage rack columns. Proc Inst Civil Eng Struct Build 2013;166:392–402.
[21] Zhang P, Alam MS. Experimental investigation and numerical simulation of pallet-rack stub columns under compression load. J Constr Steel Res. 2017;133:282–99.
[22] ANSYS®. Academic Research Mechanical. Coupled Field Analysis Guide. 18.1, ed. ANSYS, Inc: Help System; 2019.
[23] Li Z, Schafer B. Application of the finite strip method in cold-formed steel member design. J Constr Steel Res 2010;66:971–80.
[24] Li Z. Buckling analysis of the finite strip method and theoretical extension of the constrained finite strip method for general boundary conditions. Baltimore: Johns Hopkins University; 2009.
[25] Hancock GJ. Distortional Buckling of Steel Storage Rack Columns. J Struct Eng. 1985;111.
[26] AISI (American Iron and Steel Institute). Stub-Column Test Method for Effective Area of Cold-Formed Steel Columns. Washington, DC: AISI_S902; 2013.